Revealing quantum chaos with machine learning

Kharkov, Y. A.; Sotskov, V. E.; Karazeev, A. A.; Kiktenko, E. O.; Fedorov, A. K.

DOI
10.1103/PhysRevB.101.064406

Publication date
2020

Document Version
Final published version

Published in
Physical Review B

Revealing quantum chaos with machine learning

Y. A. Kharkov,[1,2,3] V. E. Sotskov,[1] A. A. Karazeev,[1,4,5] E. O. Kiktenko,[1,6,7] and A. K. Fedorov[1,4]
[1]*Russian Quantum Center, Skolkovo, Moscow 143025, Russia*
[2]*School of Physics, University of New South Wales, Sydney 2052, Australia*
[3]*Joint Center for Quantum Information and Computer Science, NIST/University of Maryland, College Park, Maryland 20742, USA*
[4]*Moscow Institute of Physics and Technology, Dolgoprudny, Moscow Region 141700, Russia*
[5]*QuTech, Delft Technical University, 2600 GA Delft, Netherlands*
[6]*Steklov Mathematical Institute of Russian Academy of Sciences, Moscow 119991, Russia*
[7]*NTI Center for Quantum Communications, National University of Science and Technology MISIS, Moscow 119049, Russia*

(Received 23 May 2019; revised manuscript received 2 December 2019; accepted 10 December 2019; published 5 February 2020)

Understanding properties of quantum matter is an outstanding challenge in science. In this paper, we demonstrate how machine-learning methods can be successfully applied for the classification of various regimes in single-particle and many-body systems. We realize neural network algorithms that perform a classification between regular and chaotic behavior in quantum billiard models with remarkably high accuracy. We use the variational autoencoder for autosupervised classification of regular/chaotic wave functions, as well as demonstrating that autoencoders could be used as a tool for detection of anomalous quantum states, such as quantum scars. By taking this method further, we show that machine-learning techniques allow us to pin down the transition from integrability to many-body quantum chaos in Heisenberg XXZ spin chains. For both cases, we confirm the existence of universal W shapes that characterize the transition. Our results pave the way for exploring the power of machine-learning tools for revealing exotic phenomena in quantum many-body systems.

DOI: 10.1103/PhysRevB.101.064406

I. INTRODUCTION

The idea of combining machin- learning methods [1] with quantum physics has stimulated intensive research activity [2]. The scope so far includes identification of quantum phases of matter and detecting phase transitions [3–15], representation of states of quantum many-body systems [16–19], and machine-learning-based analysis of experimental data [19–22].

Remarkable progress on building large-scale quantum simulators [23–26] has opened fascinating prospects for studying traditionally challenging problems of complex quantum systems, such as investigation of quantum critical dynamics and quantum chaos [27]. Quantum systems with chaotic behavior are of great interest, particularly in the view of the possibility to explore many-body quantum scars [28,29], which can be compatible with long-lived states. A standard criterion for the separation between regular and chaotic regimes uses nearest-neighbor (NN) energy-level statistics [30,31]: Poisson and Wigner-Dyson distributions correspond to integrable and chaotic systems, respectively. However, the energy-level statistics of highly excited states is not always accessible in experiments with well-controlled quantum systems.

From the machine-learning perspective, an interesting problem is to understand whether it is possible to distinguish between regular and chaotic behavior based on experimentally accessible quantities such as data from projective measurements. This question can be further extended to a possibility to detect anomalies in experimental data, such as quantum scars.

In this paper, we realize machine-learning algorithms to perform a classification between regular and chaotic states in single-particle and many-body systems. The input data contains a probability density function (PDF) representing configurations of excited states and the output is provided by two neurons, which distinguish between integrable and chaotic classes, see Fig. 1. In the single-particle case, we consider paradigmatically important models of quantum billiards. We apply an extension of a semisupervised "learning by confusion" scheme [9] to detect the integrability/chaos transition and to evaluate a critical region. We also use a clusterization technique based on a variational autoencoder (VAE) for machine learning of the transition to quantum chaos and for detection of quantum scars. The supervised approach is then extended to study the transition in Heisenberg XXZ spin-1/2 chains in the presence of additional interactions that break integrability. In our work, regular/chaos transitions are identified with the classification accuracy up to 99%. We show that our results based on the machine-learning approach are in good agreement with the analysis of level spacing distributions.

The confusion scheme is based on the assumption that the critical point λ^c exists within a given parameter range (a, b), so the data could be classified into two classes. Further, a trial critical point λ^c is proposed and all the data with parameters below λ^c are labeled as 0, and above λ^c as 1. The neural network is then trained on the entire data set for all values of λ^c, chosen from the range (a, b) with a predefined step. This method results in a universal W-like performance curve [9]. The learning by confusion scheme has been used for

the study of many-body localization–delocalization transition [32], 2D percolation and Ising models, critical behavior of the two-color Ashkin-Teller model, the XY model, the eight-state clock model [33], and exploring topological states [34].

To address the problem of revealing the transition between regular and chaotic behavior, we realized an extension of the learning by confusion scheme. At the first stage, we train the network to distinguish states belonging to the extreme cases of regular ($\lambda = 0$) and chaotic ($\lambda \sim 1$) regimes, where λ is the chaoticity parameter. By analyzing neural network outputs, we determine the critical domain where the neural network predicts a transition between the two regimes. At the second stage, we perform the standard learning by confusion protocol and we refer to the middle peak on W-like performance curves of the neural network as the transition point [9].

The paper is organized as follows. In Sect. II, we describe our machine-learning approach for classifications of chaotic/integrable wave functions in quantum billiards. We describe our supervised learning methodology and present results of neural-network-based classification of chaotic/integrable wave functions as a function of chaoticity parameter λ for three types of quantum billiards: Sinai, Bunimovich stadium, and Pascal billiards. In Sec. III, we apply an autosupervised machine-learning techinique using a VAE for clusterization analysis of quantum states in billiards. In addition, we explore applications of VAEs for anomaly detection of quantum scars and the potential of VAEs for generative modeling of regular/chaotic wave functions in quantum billiards. In Sec. IV, we apply supervised learning for detection of transition from integrability to quantum chaos in XXZ spin chains in the presence of integrability breaking interactions: next-nearest neighbor (NNN) spin-spin interaction and a local magnetic field. We draw conclusions in Sec. V. Technical details on machine-learning approaches and data set preparation are presented in the Appendixes.

II. QUANTUM BILLIARDS

Quantum billiards are among the simplest models exhibiting quantum chaos. The transition from regular to chaotic behavior in quantum billiards, which is controlled by the shape of the billiard boundary, has been intensively studied for decades [35]. Quantum billiards have been realized in various experimental setups including microwave cavities [36], ultracold atoms [37], and graphene quantum dots [38]. Quantum scars [39], which are regions with enhanced amplitude of the wave function in the vicinity of unstable classical periodic trajectories, is the hallmark of quantum chaos. Quantum scars are of a great interest in quantum billiards [39,40] and their many-body analogs have recently been studied [28,29].

We consider three standard types of two-dimensional quantum billiards: Sinai billiard, Bunimovich stadium, and Pascal's limaçon (Robnik) billiard. We define a dimensionless parameter of chaoticity λ for each billiard type, where it determines the billiard shape. In Sinai billiards, the chaoticity parameter is controlled by the ratio of the inner circle radius to the width/height of the external rectangle, so $\lambda = r/a$. In the case of Bunimovich stadium, the parameter is $\lambda = l/r$ and in the Pascal's limaçon, billiard shape is defined via the conformal map on the complex plane $D(w) : \{w = z + \lambda z^2\}$, where $|z| \leqslant 1$. At the limit of $\lambda \to 0$, these billiards have regular shapes and therefore are integrable. Varying the parameter λ allows one to trace out a continuous transition from integrability to quantum chaos.

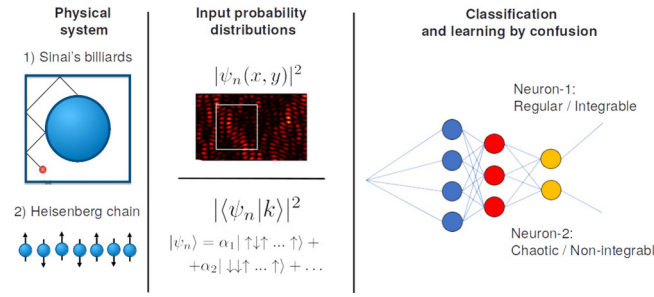

FIG. 1. Neural network approach for identifying a transition between chaotic and regular states in quantum billiards and Heisenberg spin chains. The input data contains probability distribution in the configuration space, the two neuron activation functions are used for the identification of the two regimes.

We use a supervised learning approach for revealing chaotic/regular transitions in quantum billiard models. We train a binary classifier based on a convolutional neural network (CNN) using real-space images of the PDF $|\psi_n(x, y)|^2$. The training data set consists of randomly sampled snapshots of the PDF in fragments excluding the billiard's boundary in the regions of interest. The wave functions $\psi_n(x, y)$ are obtained from the numerical solution of the stationary Schrödinger equation for the corresponding billiard type (for details see Appendixes A and B). Since the information about the transition from the regular to chaotic regimes is mostly represented in the properties of highly excited states, we use wave functions with sufficiently large values of n in our data set.

The snapshots corresponding to $\lambda = 0$ we label as regular (class 1), and snapshots corresponding to $\lambda \sim 1$ we label as chaotic (class 2). The activation function of the two neurons in the last layer allows classifying between chaotic/regular snapshots in the test data set with a high accuracy. CNN performance curves for each of the three billiard types for different values of λ show that the CNN algorithm is able to learn the difference between regular and chaotic wave functions and reveals the existence of the transition region (see Fig. 2). The CNN confidence for the binary classification

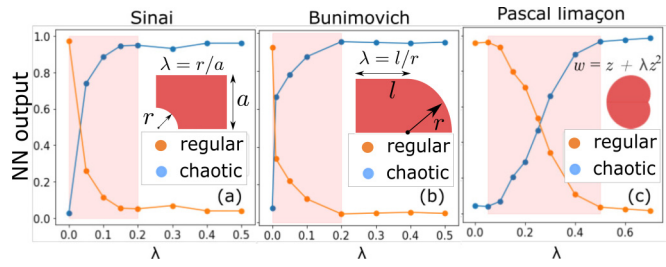

FIG. 2. Convolutional neural network outputs for (a) Sinai billiard, (b) Bunimovich stadium, and (c) Pascal's limaçon as functions of the chaoticity parameter λ characterizing the billiard's boundary shape. The highlighted critical region corresponds to the regions of "uncertainty" in neuron network output activation curves.

>95% for λ away from the critical region. The critical region determined by the CNN is highlighted in red in Fig. 2. In Sinai and Bunimovich billiards, the critical region detected by the CNN algorithm is $0 < \lambda_c < 0.2$. The detected critical region for the Pascal billiard is $0.05 < \lambda < 0.5$. The boundaries of the critical regions provided by the CNN classifier are in good agreement with the ones obtained from the analysis of the energy-level spacing statistics, see Appendix C.

The critical region can be analyzed in more detail within the learning by confusion scheme [9] by performing a dynamical reassignment of the class labels with respect to a given value of λ. We note that a precise definition of the transition point λ_c is somewhat ambiguous and depends on selected criteria because all observables have a smooth dependence on the parameter λ. Therefore, in our approach, we only estimate the location of a characteristic critical point λ_c, separating regular and chaotic regimes. The estimated position of the critical point is $\lambda_c \approx 0.1$ in Sinai billiards and $\lambda_c \approx 0.2$ in Pascal limaçon billiards. The location of the critical point λ_c in Pascal's billiard agrees with Ref. [41]. We note that the analysis of the chaotic/regular transition for the Bunimovich stadium is challenging due to its extreme sensitivity to the variation of the chaoticity parameter λ (see Ref. [40]).

One of the key features that allows us to perform machine learning of the regular-to-chaos transition is the difference in statistical properties of $|\psi_n|^2$ in these two regimes. While in the chaotic case the wave functions have Gaussian statistics, in the regular case the probability distribution is nonuniversal and has a power-law singularity at small values of ψ_n [42].

The standard approach to identify a transition from an integrability to a quantum chaos is based on the comparison of the energy-level spacing statistics with the Poisson distribution and the Wigner-Dyson distributions. To characterize a "degree of chaoticity" of the system, one can use the average ratio of consecutive level spacings $\langle r \rangle$, where $r = \min(\Delta E_{n+1}, \Delta E_n)/\max(\Delta E_{n+1}, \Delta E_n)$ and $\Delta E_n = E_n - E_{n-1}$ [43]. Here we introduce a different measure based on the Kullback-Leibler (KL) divergence, defined as follows:

$$D_{\mathrm{KL}}(P_\lambda||P') = \int_0^\infty P_\lambda(s) \log \frac{P_\lambda(s)}{P'(s)} ds, \qquad (1)$$

where $P_\lambda(s)$ is the level spacing distribution for a given value of λ and $P'(s)$ is the Wigner-Dyson or Poisson distribution: $P'_{\mathrm{Pois}} = e^{-s}$, $P'_{\mathrm{WD}} = \frac{\pi}{2} s \exp(-\frac{\pi}{4} s^2)$. Here s is the unfolded NN energy-level spacing.

In the critical region between regular and chaotic regimes, the energy spacing distribution is neither Poisson nor Wigner-Dyson. There exists a point λ_c when P_{λ_c} is equidistant from both Poisson and Wigner-Dyson distributions within the KL metric, $D(P_{\lambda_c}||P'_{\mathrm{Pois}}) = D(P_{\lambda_c}||P'_{\mathrm{WD}})$, which we refer to as a critical point. The critical points predicted by the confusion scheme and KL divergence curves are in good agreement. We note that the confusion scheme uses experimentally accessible quantities, whether energy-level statistics from experimental data is hardly accessible in condensed matter and atomic simulator experiments.

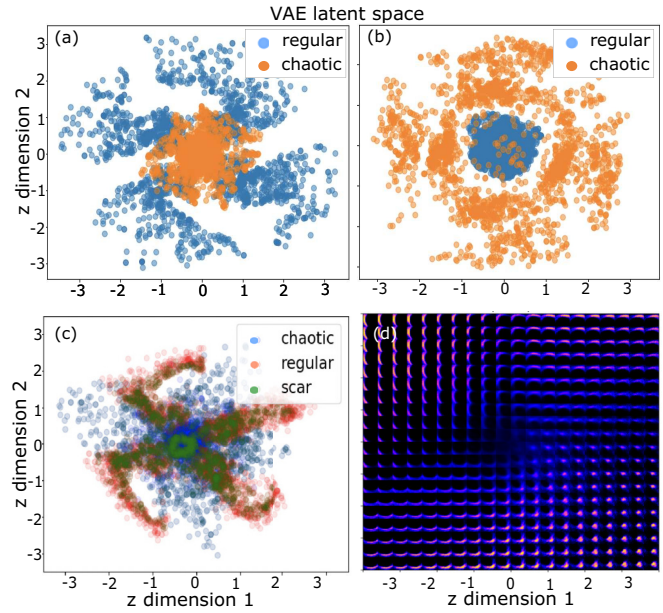

FIG. 3. Autosupervised learning of regular and chaotic states in quantum billiards with variational autoencoder (VAE). Latent space representation of the wave functions in (a) Bunimovich stadium, (b) Sinai billiard; $z_{1,2}$ are coordinates in the two-dimensional latent space. (c) Anomaly detection: Latent space representation of wave functions corresponding to regular (red dots, $\lambda = 0$) and chaotic (blue dots, $\lambda = 0.4$) wave functions as well as scarred chaotic wave functions (green dots) in Bunimovich billiard. (d) VAE as a generative model: Images of wave functions $|\psi|^2$ generated by VAE corresponding to different positions in the latent space variables (z_1, z_2) (Pascal billiard). By continuously scanning across two-dimensional latent space, the VAE performs a smooth interpolation between wave functions from chaotic and regular wave functions.

III. VAE AND ANOMALY DETECTION IN QUANTUM BILLIARDS

An alternative approach to differentiate between regular and chaotic regimes is to use autosupervised machine-learning techniques, such as VAEs. VAEs are generative NN models that are able to directly learn statistical distributions in raw data and can be efficiently used for solving clustering problems [44,45]. VAEs consist of encoding NN, latent space and decoding NNs, Fig. 3(a). During the training, VAE "learns" to reproduce initial data by optimizing the weight in the encoder and decoder NNs and parameters in the latent layer. Training VAEs on the images with $|\psi_n(x, y)|^2$ corresponding to regular ($\lambda = 0$) and chaotic ($\lambda \sim 1$) cases and by taking samples from the latent space with the dimension 2 results in two clearly separated clusters representing regular and chaotic wave functions. For details on VAE architecture and optimization, see Appendix D.

In Figs. 3(a) and 3(b), we demonstrate latent space representation of wave functions in Bunimovich and Sinai billiards. The separation in the two clusters shows that VAE is able to learn the difference in the statistical properties of $|\psi_n|^2$ in regular and chaotic billiards. A similar approach was used for unsupervised learning of phase transitions [4].

In addition to the autosupervised learning of regular/chaotic quantum states, VAEs could be used as a tool for anomaly detection in quantum data, in particular, identification of scarred wave functions. In this context, we use the term anomalous to describe a subset of samples with statistical properties drastically different from the statistical properties of the entire data set. Data-driven anomaly detection with VAEs arises in machine learning, data mining, and cybersecurity applications [46–49]. Applications of VAE-based anomaly-detection methods were recently studied in the context of classical phase transitions [50] and detection of elementary particles [51]. However, the potential of anomaly-detection methods in quantum systems has been mostly unexplored. Anomalous samples could be detected using latent space representation $z_{1,2}$ as a set—a cloud of points falling outside of the chaotic cluster (for additional details, see Appendix E). Using a pretrained VAE, we generate a set of points in the latent space corresponding to the scarred chaotic wave functions, see Fig. 3(c). The anomalous cluster representing scarred wave functions falls outside of the chaotic cluster and has a large overlap with a regular cluster. This unusual behavior indicates similarity between scarred wave functions and wave functions in integrable billiards. An interesting extension of this approach could be VAE-based anomaly detection method for identification of quantum many-body scars.

Another additional feature of VAEs is the ability to smoothly interpolate between data sets corresponding to the two classes. In Fig. 3(d), we show wave functions generated by VAE in Pascal billiard via scanning across the two-dimensional latent space $z_{1,2}$. This procedure allows us to perform continuous interpolation between chaotic (center region) and regular wave functions (outer region). VAE-based generative modeling of quantum states could give rise to new approaches in simulations of quantum systems [52] as well as for new applications in the context of quantum chaos. Exploring a full potential of unsupervised machine-learning methods for clustering quantum states is beyond the scope of the present paper.

IV. DETECTION OF QUANTUM CHAOS IN XXZ SPIN CHAINS

While quantum billiards is an instructive example of a single-particle quantum chaos, quantum chaotic regimes in many-body systems are more interesting. Developing machine-learning approaches to characterize/classify many-body states in chaotic and integrable regimes using only limited information from measurements is a nontrivial task. For example, such techniques can benefit from the analysis of experimental data from quantum simulators [23–26]. As a prototypical example of a quantum many-body integrable system, we consider 1D Heisenberg XXZ spin chain, which is of great interest for realizing models of quantum magnetism using quantum simulators [53]. Recent experimental advances have opened exciting prospects for exploiting a rich variety of tunable interactions in Rydberg atoms [25,54–57] and cold polar molecules [58–60] for engineering of spin Hamiltonians including the XXZ model.

The Hamiltonian of the Heisenberg XXZ model reads

$$H_{\mathrm{XXZ}} = \sum_{i=1}^{N-1} \left[J\left(S_i^x S_{i+1}^x + S_i^y S_{i+1}^y\right) + J_{zz} S_i^z S_{i+1}^z \right], \qquad (2)$$

where N is the number of spins, J and J_{zz} are the Heisenberg exchange constants, and $S_i^{x,y,z}$ are Pauli spin-1/2 operators. For simplicity, we only consider an antiferromagnetic XXZ model, $J, J_{zz} > 0$. Hereafter, we set $J = 1$. The XXZ model is integrable and exactly solvable by Bethe ansatz [58], however, it can be nonintegrable in the presence of additional interactions.

Here we consider two types of perturbations that violate integrability of the XXZ model: (i) antiferromagnetic NNN spin-spin interaction and (ii) a local static magnetic field acting on a single spin (impurity). We parametrize perturbations to the Hamiltonians in the following form:

$$\text{(i)}: \; H' = \lambda \sum_{i=1}^{N-2} S_i^z S_{i+2}^z, \quad \text{(ii)}: \; H' = \lambda S_{(N+1)/2}^z. \qquad (3)$$

We consider spin chains with an odd number of spins N, so in case (ii) the local magnetic field is acting on the spin in the middle of the chain, i.e., $i = (N+1)/2$. The Hamiltonian of the perturbed XXZ model reads

$$H = H_{\mathrm{XXZ}} + H'. \qquad (4)$$

We train a multilayer perceptron (MLP) on the data set containing the probabilities $|\langle \psi_n | k \rangle|^2$ of the spin configurations in S_z representation ($|k\rangle$ refers to basis states in S_z representation), e.g., $|\uparrow\downarrow \ldots \downarrow\rangle$. The eigenfunctions $|\psi_n\rangle$ are obtained by exact diagonalization of spin-chain Hamiltonian (for details, see Appendix F); here we consider system size $N = 15$. Similarly to the case of quantum billiards, we consider only highly excited states with n corresponding to the levels lying in the middle of the energy spectrum, $E_n \approx 0$.

To pin down the chaos/integrability transition, we use a MLP NN, see details in Appendix G. We evaluate NN classification prediction for the test data set as a function of λ, see Fig. 5(a), the critical region is highlighted with red. For XXZ + NNN (Fig. 4) and XXZ + impurity (Fig. 5), detected critical regions are $0.05 \leqslant \lambda_c \leqslant 0.175$ and $0.05 \leqslant \lambda_c \leqslant 0.125$, respectively, which turn out to be in agreement with level spacing distributions represented in Fig. 4(b), see Appendix C and within the range of values obtained in previous works [61–63]. Within these critical regions, learning by confusion resulted in W-like performance curves [see Fig. 4(c) and Appendix H], and detected transition points $\lambda_c \approx 0.1$ for XXZ + NNN and $\lambda_c \approx 0.085$ for XXZ + impurity. We note that we have a reasonable agreement with the results based on the KL divergence calculations.

V. CONCLUSIONS

In summary, we have shown the potential of classical supervised and unsupervised machine-learning techniques for classification of regular/chaotic regimes in single-particle and many-body systems. For quantum billiards and XXZ spin chains, we demonstrated that neural networks can serve as a binary classifier to distinguish between the two regimes with remarkably high accuracy. We revealed the integrability-chaos critical region purely based on machine-learning techniques

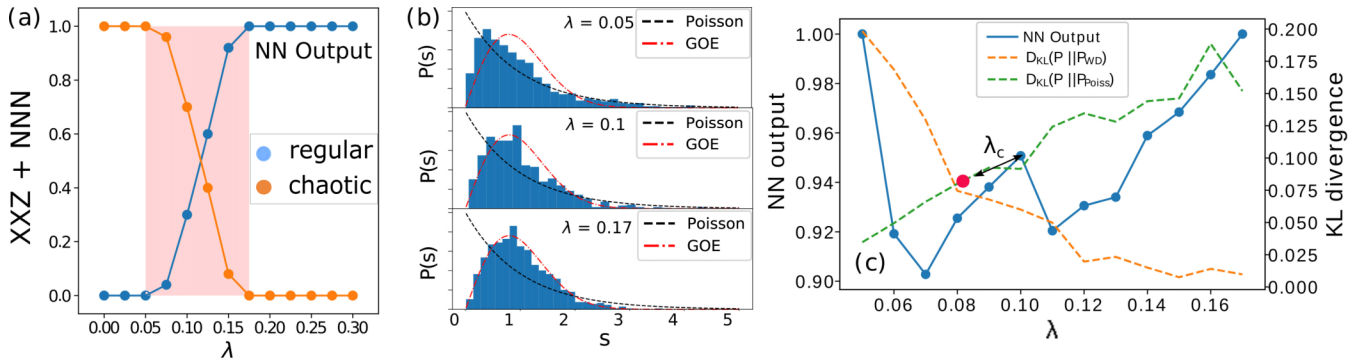

FIG. 4. Neural network classification accuracy between integrable and chaotic XXZ spin chains with the next-nearest-neighbor interactions for $N = 15$ spins ($J_{zz} = 1$). (b) Distribution of energy-level spacings and the Poisson/Wigner-Dyson distributions. Plots correspond to XXZ model. (c) Learning by confusion W-like NN performance curve.

and located the transition point using the learning by confusion approach. The extension of our work opens an avenue to study chaotic and integrable regimes and detect quantum anomalies using experimentally accessible data in different many-body quantum systems, including atomic simulators. Harnessing machine-learning methods could open up exciting possibilities for studying exotic many-body phenomena with controlled quantum many-body systems, such as many-body localization [64], many-body quantum scars [28], and ergodic/nonergodic phase transitions [65] and near-critical properties of these systems.

ACKNOWLEDGMENTS

We are grateful to M.B. Zvonarev and V.V. Vyborova for valuable suggestions. We thank G.V. Shlyapnikov, V.I. Yudson, and B.L. Altshuler for fruitful discussions and useful comments. The initial stage of the work was supported by RFBR (Grant No. 18-37-00096). The work on the extension of results on the anomaly detection and applications to many-body systems was supported by RSF (No. 19-71-10092).

APPENDIX A: NUMERICAL SOLUTION OF THE SCHRÖDINGER EQUATION FOR QUANTUM BILLIARDS

We solve a stationary Schrödinger equation describing a single particle in a quantum billiard with the Dirichlet boundary condition,

$$-\frac{\hbar^2}{2m}\nabla^2\psi_n = E_n\psi_n, \quad \psi_n|_{\partial D} = 0, \tag{A1}$$

where $\psi_n(x, y)$ is the wave function and E_n is the energy of a particle in the billiard with the boundary ∂D; $\nabla^2 = \partial_{xx} + \partial_{yy}$ is the two-dimensional Laplace operator. Hereafter, we set the Plank's constant and the mass to unity, $\hbar = m = 1$. To solve Eqs. (A1) for an arbitrary 2D billiard boundary shape, we use MATLAB PDE toolbox. The PDE solver is based on the finite element method with an adaptive triangular mesh for a given boundary geometry. To reduce computational complexity and to avoid additional complications due to degeneracies of eigenstates, we constrain the eigenfunctions to a specific symmetry (parity) sector. We remove degeneracies by considering the lowest symmetry segments of billiards. In the case of the Bunimovich stadium, we consider a quarter of the billiard [see inset of Fig. 1(b) in the main text]. For the Sinai billiard, we consider a boundary with the incommensurate ratio of vertical and horizontal dimensions of the external rectangle, $a_x/a_y = \sqrt{5}/2$ (we denote $a \equiv a_x$ in the main text). In the case of the Pascal limaçon billiard, the degeneracy is lifted when considering only the upper part of the billiard $\mathrm{Re}(z) \geqslant 0$.

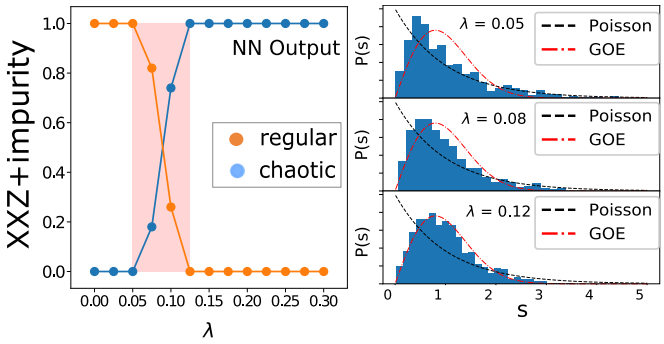

FIG. 5. Left panel: NN classification accuracy for chaos-integrability transition in XXZ model in the presence of a local magnetic field (a magnetic impurity) for $N = 15$ spins. Right panel: Energy-level spacing distributions for different values of λ.

APPENDIX B: DATA-SET PREPARATION AND CNN FOR QUANTUM BILLIARDS

Wave functions $\psi_n(x, y)$ obtained from numerical solution of the Schrödinger equation are converted into images of PDFs $|\psi_n(x, y)|^2$. From original images with ~500 × 500 pixels, we randomly select square fragments (region of interest) which exclude the billiard boundary, ~300 × 300 pixels. To reduce the size of the images, we perform a coarse graining (downsampling) to images with dimensions 36 × 36. The data set for each billiard type contains wave functions corresponding to high energy states, $470 \leqslant n < 500$. To increase the amount of images in the data set, we perform an augmentation of the data set by adding horizontal and vertical reflections, discrete rotations by angles $\alpha = k\pi/2$, and rotations by random angles from the uniform distribution $\alpha \in [-25^o, 25^o]$. The total number of images in the resulting data set for each billiard type and each value of λ is $M = 4000$. The trial

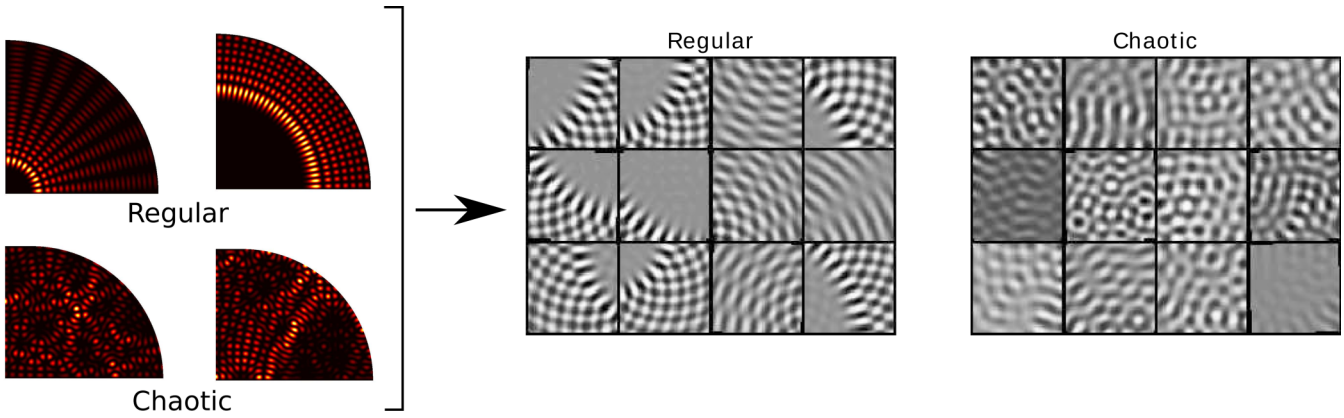

FIG. 6. Sample images of $|\psi(x, y)|^2$ in the data set for Bunimovich billiard. Regular case ($\lambda = 0$) and chaotic case ($\lambda = l/r = 0.2$).

samples from the data set for the Bunimovich billiard are shown in Fig. 6.

The training data set consists of labeled images from class 1 (regular, $\lambda = 0$) and class 2 (chaotic, $\lambda = \lambda_0$). The value of λ_0 we independently choose for each billiard type: Sinai—$\lambda_0 = 0.4$, Bunimovich—$\lambda_0 = 0.2$, Pascal—$\lambda_0 = 0.8$. To check that at $\lambda = \lambda_0$ the system is in the chaotic regime, we compare the energy-level spacing distribution with the Wigner-Dyson distribution. As long as the value of λ_0 is much greater than the critical λ, $\lambda_0 \gg \lambda_c$, the NN activation curves remain practically unchanged (see Fig. 1 in the main text).

The training and test data sets are split in the proportion 70%/30%. The test set for each billiard type consists of images for several values of λ (including values of λ not present in the training data set), evaluation of the NN output for the sample images from the test data set for each value of λ results in the NN prediction curves presented in Fig. 1 in the main text.

A CNN consists of two convolutional layers followed by pooling fully connected and final softmax layers. The output from the second convolutional layer is subject to dropout regularization and batch normalization. The cost function for the binary classifier is the cross entropy and the neuron activation function is ReLU. The scheme of the CNN architecture is presented in Fig. 7. The weights in the CNN are optimized with the use of the Adam optimizer. The batch size is 60, the number of training epochs is of about 500, the learning rate is $\alpha = 5 \times 10^{-4}$.

APPENDIX C: ENERGY-LEVEL SPACING STATISTICS IN QUANTUM BILLIARDS

We validate results of NN classification prediction in quantum billiards (Pascal limaçon, Sinai and Bunimovich billiards) by comparing NN predictions with the energy level spacing distributions, see Fig. 8. In the regular case the energy-level spacing distribution $P(s)$ is close to the Poisson distribution (black dashed line), and in the chaotic case $P(s)$ is approaching the Wigner-Dyson distribution (red dashed dotted line).

APPENDIX D: UNSUPERVISED LEARNING WITH VAE

We perform unsupervised (autosupervised) learning of two classes (regular and chaotic) using a VAE. The unlabeled data set was prepared in a similar way as for the supervised learning. The data set consists of randomly sampled images of $|\psi_n(x, y)|^2$ with the dimensions 36×36, the number of samples in the training data set for each billiard type is 6×10^3, number of testing samples is 2×10^3 for each billiard type. A VAE was trained and tested for the states with $n \sim 500$ in Bunimovich and Sinai's billiards, $\lambda = 0$ corresponds to the regular class, $\lambda = 0.4$ corresponds to the chaotic class. VAE consists of the encoder $Q_\theta(x_i)$, decoder $P_{\theta'}(z_i)$, Gaussian sampler G_{μ_j,σ_j}, and the latent space of dimension 2 (latent space parameters $\mu_{1,2}$ and $\sigma_{1,2}$) representing the two classes, regular and chaotic, the architecture of VAE is shown in Fig. 9. Here x_i is the vectorized representation of the input data

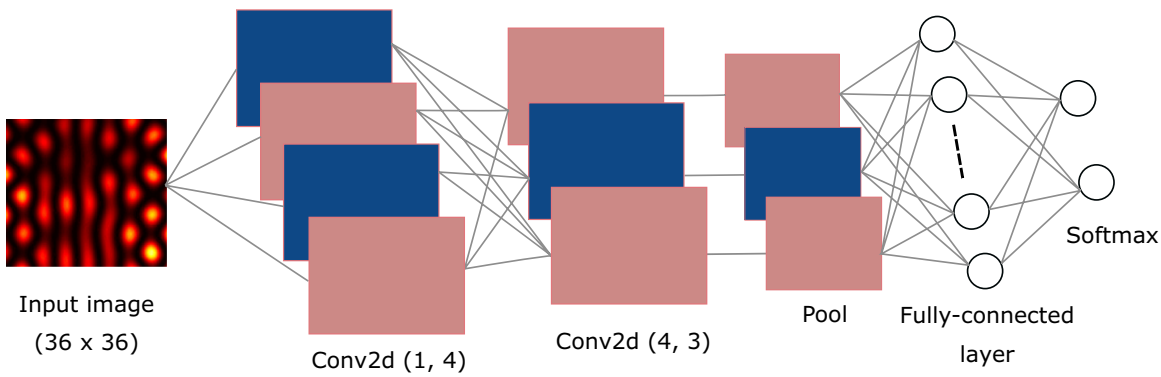

FIG. 7. CNN used for recognizing chaotic regimes in quantum billiards.

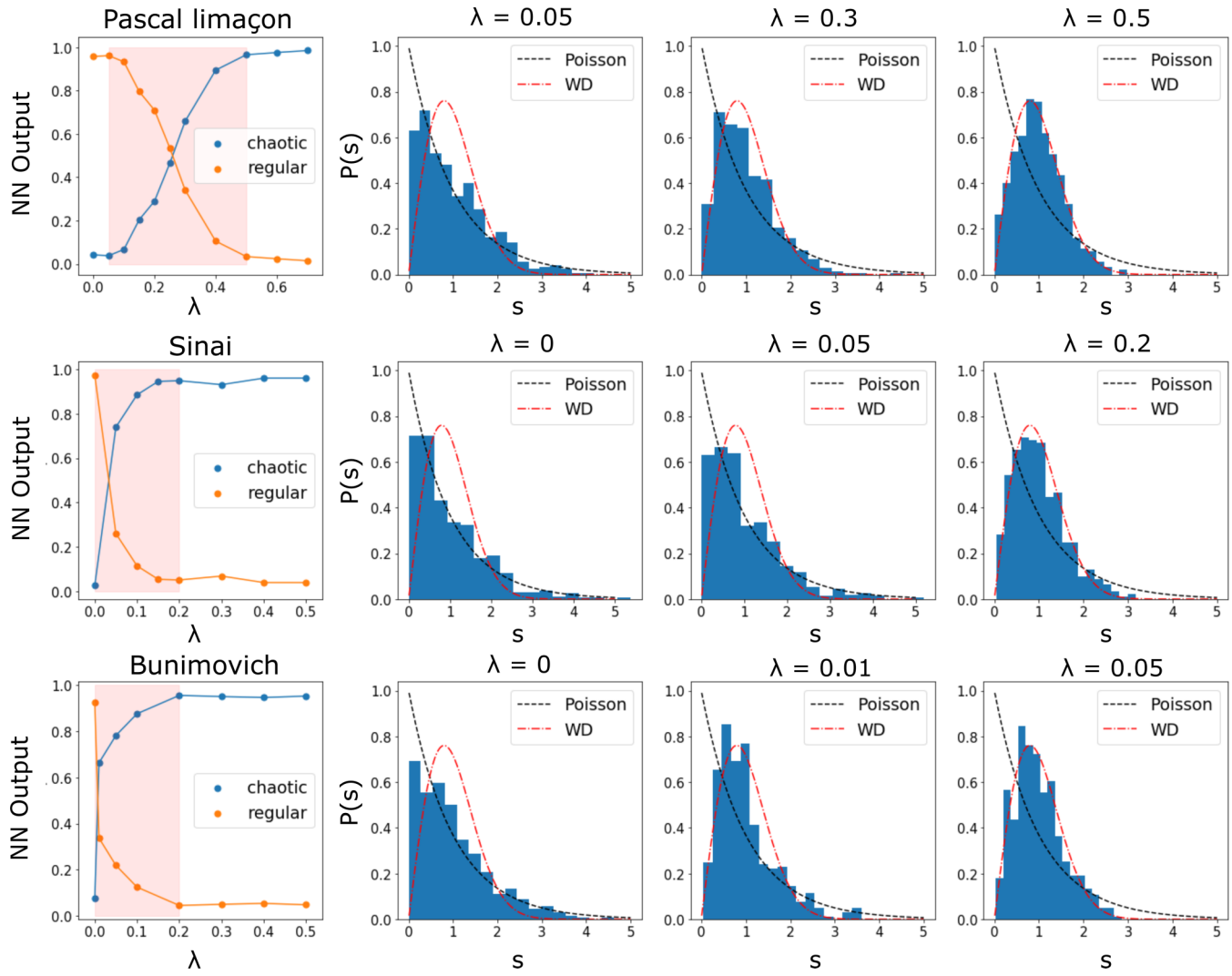

FIG. 8. Left column: The CNN activation functions (Fig. 1 from the main text). The histograms show the energy-level spacing distributions (lowest 500 energy levels). To compare NN predictions for the regular-to-chaos critical region, we compare the energy-level spacing distribution with the standard Poisson/GOE distributions.

(image), θ (θ') are NN parameters of the encoder (decoder). The sampler generates random latent space variables $z_{1,2}$ with the mean $\mu_{1,2}$ and the dispersion $\sigma^2_{1,2}$. The decoder performs reconstruction from the latent space representation to the original data format, the image $|\psi(x,y)|^2$ with dimensions equal to the input dimension (36×36). The final layer of the decoder has sigmoid activation function to match the input

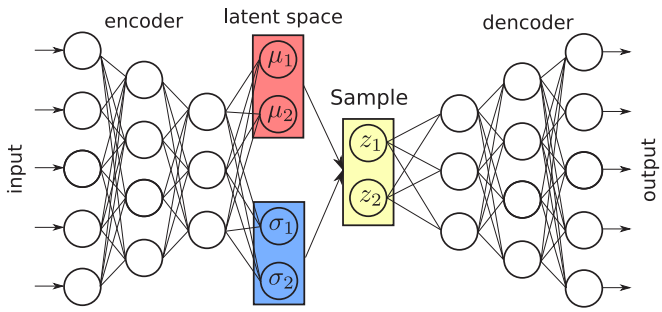

FIG. 9. Architecture of variational autoencoder (VAE) for unsupervised learning of regular-chaos transition in quantum billiards.

data range (we normalize the input data so $\max\{|\psi(x,y)|^2\} = 1$. The encoder and decoder are represented by a fully connected NN with two hidden layers and $N_h = 150$ neurons in each layer. The structure of the decoder network replicates the structure of the encoder (number of layers, number of neurons, activation function) and the decoder is a "mirrored" replica of the encoder. The encoder network is given by two fully connected layers with ReLU activation function between the layers.

The objective function is a sum of reconstruction loss (binary cross entropy) and KL divergence loss [45],

$$\mathcal{L}_{\rm VAE}(x) = \mathbb{E}_{z\sim Q_\theta(x)}[\log P_{\theta'}(z)] - \frac{1}{2}\sum_{j=1,2}\left(1 + \log\sigma_j^2 - \mu_j^2 - \sigma_j^2\right), \quad \text{(D1)}$$

where $\mathcal{L}_{\rm VAE}$ is the loss function, x is the data sample (discretized wave function image $|\psi|^2$), and $P_{\theta'}$ is the output of the decoder network. The expectation value $\mathbb{E}_{z\sim Q_\theta(x)}[\ldots]$ is evaluated by averaging over batch z_j sampled from the latent space. The objective function Eq. (D1) is also known

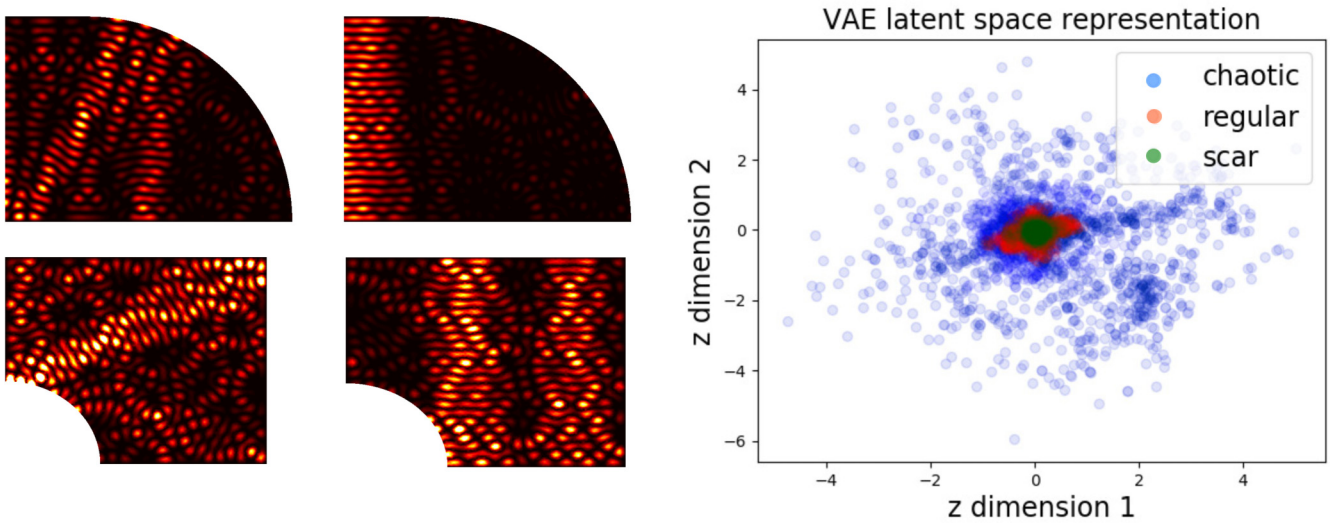

FIG. 10. Left panel: Examples of scarred wave functions in Bunimovich and Sinai billiards used for quantum anomaly detection. Right panel: Latent space distribution of VAE for regular ($\lambda = 0$) and chaotic ($\lambda = 0.4$) wave functions in Sinai billiard. Green dots correspond to scared wave functions.

as the variational lower bound or evidence lower bound. This is the bound on the log probability to observe a data point x, therefore by maximizing the lower bound Eq. (D1) we maximize the log-likelihood probability of observation x. We implemented VAE within PyTorch framework. VAE was trained over 50 epochs using an Adam optimizer [66], learning rate is $\alpha = 10^{-4}$, batch size is 40 samples.

APPENDIX E: ANOMALY DETECTION WITH VAE AND QUANTUM SCARS

Among the wave functions of Sinai and Bunimovich billiards, we selected states with scarred wave functions. The total number of scarred wave functions constituted only a small fraction of the entire data set (<5%). Some typical examples of scarred wave functions in Bunimovich and Sinai billiards are shown in the left panel of Fig. 10. We train VAE on the entire data set containing chaotic and regular wave functions. At test time, we feed real space images of wave function snapshots $|\psi_n(x, y)|$ to VAE and analyze the latent space representaion $z_j \sim G_{\mu_j,\sigma_j}[Q_\theta(x_i)]$ of the input samples x_i. The portion of "scarred" samples in the test data set is 33%, such ratio was chosen to make scarred clusters in the latent space quite visible.

Scarred chaotic wave functions form a cluster in the "wrong" region that strongly overlaps with the regular cluster, see Fig. 10, right panel and Fig. 2(c) in the main text. This is a signature of anomalous properties of scarred wave functions that we use as a case for demonstration of the anomaly detection approach. In Fig. 10 (right panel), we show how regular ($\lambda = 0$), chaotic ($\lambda = 0.4$), and scarred wave functions ($\lambda = 0.4$) of Sinai billiards are represented in the VAE's latent space. Another popular VAE-based approach for anomaly detection relies on the increase of VAE reconstruction loss (or reconstruction probability) of anomalous data [49]. This approach does not pertain to our case, because the reconstruction loss for scarred wave functions is approximately equal to the reconstruction loss for regular wave functions.

In addition to anomaly detection, we use VAE latent space representation to explore possibility of smooth interpolation between wave functions corresponding to regular and chaotic billiards. By scanning across coordinates in the latent space z_1, z_2 and decoding the latent representation with the decoder neural network $y \sim P_{\theta'}(z)$ into vectorized form corresponding to the original data dimensions, we obtained "images" of wave functions $|\psi|^2$ [Fig. 2(d), main text] interpolating between chaotic (center region) and regular wave functions (outer region).

APPENDIX F: DATA-SET PREPARATION FOR HEISENBERG XXZ CHAINS (EXACT DIAGONALIZATION)

We find eigenstates of Heisenberg XXZ model for an arbitrary value of perturbation parameter λ by the exact diagonalization method based on the Lancsoz algorithm [67]. We used Python implementation of the QuSpin software package [68]. To avoid extensive computational costs, the size of the Hamiltonian matrix was reduced by considering only the eigenstates in certain parity and magnetization sectors of the XXZ Heisenberg model. Specifically, we find eigenstates in the even parity sector and the lowest magnetization sector. The lowest magnetization sector corresponds to the states with $m_z = (n_\uparrow - n_\downarrow)/2 = 1/2$ (for odd spin chains), where $n_\uparrow$ and $n_\downarrow$ are the number of up and down spins, respectively.

The data set for Heisenberg XXZ chains consists of vectors of probability densities (PDs) $|\langle\psi_n|k\rangle|^2$ corresponding to integrable and chaotic Hamiltonians. We take the wave function $|\psi_n\rangle$ corresponding to a quantum state with the energy lying in the center of the spectrum. To prepare a diverse data set for a given value of λ, we randomly select J_{zz} from the uniform distribution $J_{zz} \in [0.8, 2]$. Since the XXZ model is integrable for any value of J_{zz}, we build a data set corresponding to a set of different Hamiltonians by varying J_{zz}. In the training set, we include PDs for regular systems ($\lambda = 0$) and chaotic systems ($\lambda_0 = 0.3$) and label the samples accordingly. The test set contains PDs corresponding to a discrete set of λ lying in the

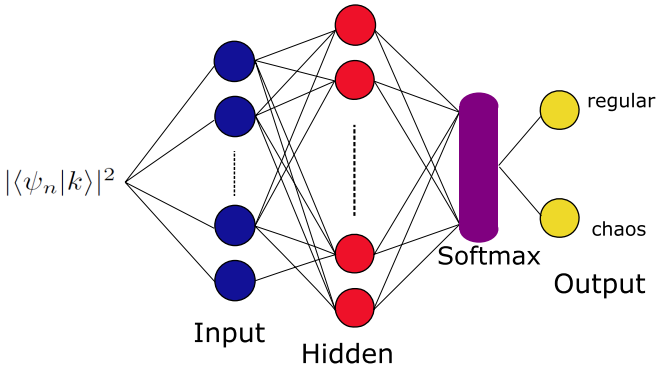

FIG. 11. Multilayer perceptron used for investigation integrable/chaotic transitions in Heisenberg XXZ chains.

interval $\lambda \in [0, 0.3]$. The training set contains 400 samples, the testing set consists of 100 samples.

APPENDIX G: MULTILAYER PERCEPTRON

We use a standard MLP neural network that consists of an input layer with the size n, which is equal to the size of vector with PDs in the specified symmetry (parity and total magnetization) sector of the eigenstates; one hidden layer with $m = 700$ neurons and an output softmax layer. Neurons of the hidden layer receive input x_i and a weight w_{xi} $(i = 1...n)$ and compute output $y = f(z)$, where $z = \sum_{i=1}^{n} x_i w_{xi}$. An output of a neuron is computed with a sigmoid activation function $f(z) = 1/(1 + e^{-z})$. Further, each output y with a corresponding weight w_{yi} $(i = 1...m)$ is passed to two neurons of an output softmax layer, which finally results in a two-component vector (p_1, p_2) that obeys the constraint $p_1 + p_2 = 1$. The softmax layer for binary classification task is defined as $p_{j=1,2} = \frac{\exp y_j}{\sum_{i=1,2} \exp y_i}$. The scalar values p_1 (p_2) are interpreted as a probability that the input wave function belongs to the regular (chaotic) class. The objective function is the binary cross entropy. Neural network weights are optimized using an Adam optimizer [66] with the learning rate $\alpha = 0.001$, batch size of 10 samples, 20 training epochs. The scheme of the neural network architecture is presented in Fig. 11.

We used a densely connected MLP instead of CNN architecture due to the following reason: CNN is designed to grasp spatial structure of the input data, whereas MLPs are used for more general tasks. CNN architecture is very natural for image recognition tasks (in our case, classifying wave functions in quantum billiards), but generically is not a natural representation for the case of the spin chains, where the input data corresponds to the components of the many-body wave function.

APPENDIX H: DETECTION OF CRITICAL POINTS WITH A CONFUSION SCHEME WITH CONFUSION METHOD (W-SHAPE CURVES)

W-like neural network performance curves versus chaoticity parameter λ found by a learning by confusion approach

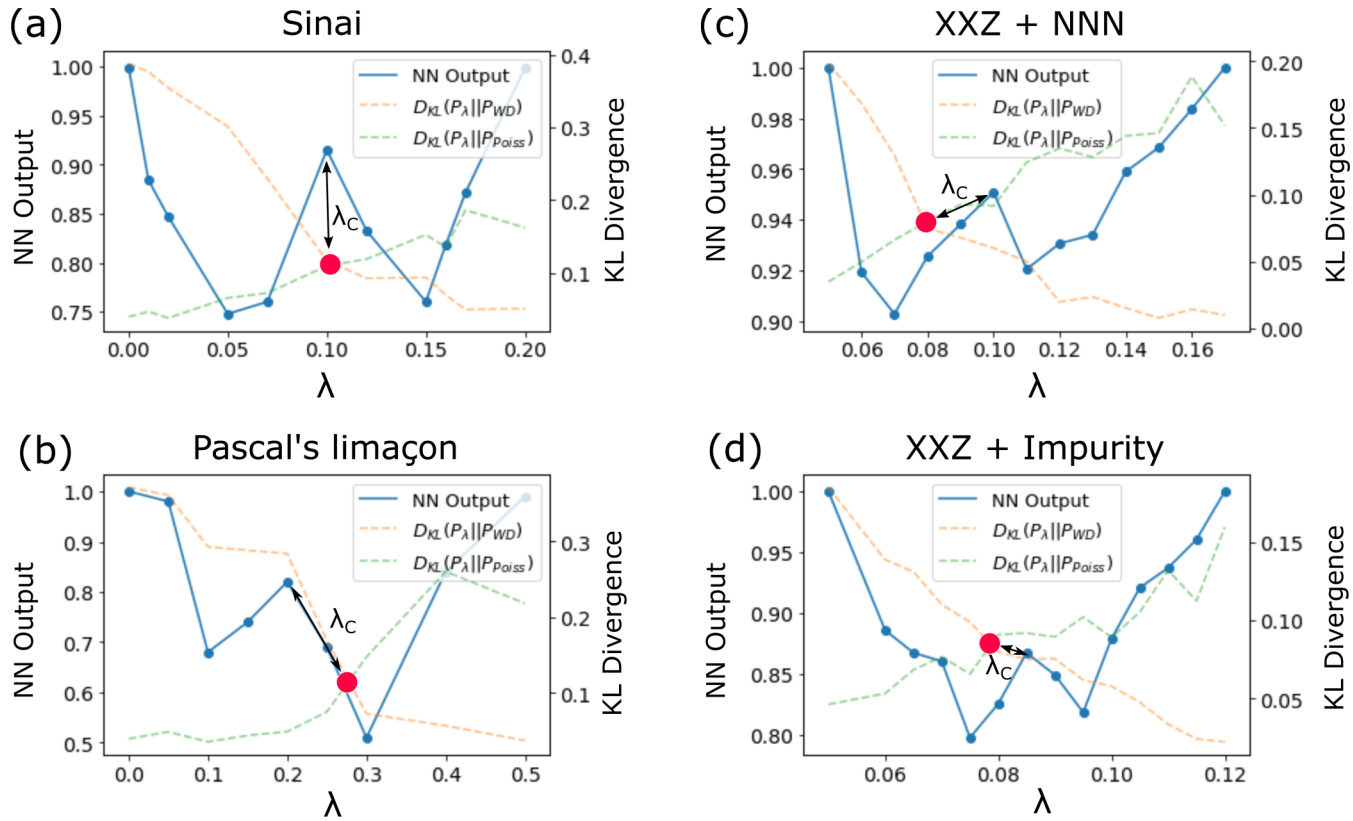

FIG. 12. Universal W-like NN performance curves in the learning by confusion scheme for the Sinai billiard (a), the Pascal's limaçon (b), XXZ + NNN (c), and XXZ + Impurity (d). The predicted transition point λ_c is highlighted. The estimated position of the transition point predicted from the KL divergence calculation is shown with a red dot.

for quantum billiards and XXZ spin chains are shown in Fig. 12. The central peak of the W-like curve corresponds to the transition point λ_c predicted by the neural network.

[1] Y. LeCun, Y. Bengio, and G. Hinton, Deep learning, Nature (London) **521**, 436 (2015).

[2] J. Biamonte, P. Wittek, N. Pancotti, P. Rebentrost, N. Wiebe, and S. Lloyd, Quantum machine learning, Nature (London) **549**, 195 (2017).

[3] L. Wang, Discovering phase transitions with unsupervised learning, Phys. Rev. B **94**, 195105 (2016).

[4] S. J. Wetzel, Unsupervised learning of phase transitions: From principal component analysis to variational autoencoders, Phys. Rev. E **96**, 022140 (2017).

[5] J. Carrasquilla and R. G. Melko, Machine learning phases of matter, Nat. Phys. **13**, 431 (2017).

[6] P. Broecker, J. Carrasquilla, R. G. Melko, and S. Trebst, Machine learning quantum phases of matter beyond the fermion sign problem, Sci. Rep. **7**, 8823 (2017).

[7] F. Schindler, N. Regnault, and T. Neupert, Probing many-body localization with neural networks, Phys. Rev. B **95**, 245134 (2017).

[8] K. Ch'ng, J. Carrasquilla, R. G. Melko, and E. Khatami, Machine Learning Phases of Strongly Correlated Fermions, Phys. Rev. X **7**, 031038 (2017).

[9] E. P. L. van Nieuwenburg, Y.-H. Liu, and S. D. Huber, Learning phase transitions by confusion, Nat. Phys. **13**, 435 (2017).

[10] M. Koch-Janusz and Z. Ringel, Mutual information, neural networks and the renormalization group, Nat. Phys. **14**, 578 (2018).

[11] M. J. S. Beach, A. Golubeva, and R. G. Melko, Machine learning vortices at the Kosterlitz-Thouless transition, Phys. Rev. B **97**, 045207 (2018).

[12] J. Greitemann, K. Liu, and L. Pollet, Probing hidden spin order with interpretable machine learning, Phys. Rev. B **99**, 060404 (2019).

[13] A. Bohrdt, C. S. Chiu, G. Ji, M. Xu, D. Greif, M. Greiner, E. Demler, F. Grusdt, and M. Knap, Classifying snapshots of the doped Hubbard model with machine learning, Nat. Phys. **15**, 921 (2019).

[14] K. Liu, J. Greitemann, and L. Pollet, Learning multiple order parameters with interpretable machines, Phys. Rev. B **99**, 104410 (2019).

[15] X.-Y. Dong, F. Pollmann, and X.-F. Zhang, Machine learning of quantum phase transitions, Phys. Rev. B **99**, 121104 (2019).

[16] G. Carleo and M. Troyer, Solving the quantum many-body problem with artificial neural networks, Science **355**, 602 (2017).

[17] I. Glasser, N. Pancotti, M. August, I. D. Rodriguez, and J. I. Cirac, Neural-Network Quantum States, String-Bond States, and Chiral Topological States, Phys. Rev. X **8**, 011006 (2018).

[18] S. Lu, X. Gao, and L.-M. Duan, Efficient representation of topologically ordered states with restricted Boltzmann machines, Phys. Rev. B **99**, 155136 (2019).

[19] G. Torlai, G. Mazzola, J. Carrasquilla, M. Troyer, R. Melko, and G. Carleo, Neural-network quantum state tomography, Nat. Phys. **14**, 447 (2017).

[20] T. Sriarunothai, S. Wölk, G. S. Giri, N. Friis, V. Dunjko, H. J. Briegel, and C. Wunderlich, Speeding-up the decision making of a learning agent using an ion trap quantum processor, Quantum Sci. Technol. **4**, 015014 (2019).

[21] Y. Zhang, A. Mesaros, K. Fujita, S. D. Edkins, M. H. Hamidian, K. Chng, H. Eisaki, S. Uchida, J. C. Séamus Davis, E. Khatami, and E.-A. Kim, Machine learning in electronic-quantum-matter imaging experiments, Nature (London) **570**, 484 (2019).

[22] B. S. Rem, N. Käming, M. Tarnowski, L. Asteria, N. Fläschner, C. Becker, K. Sengstock, and C. Weitenberg, Identifying quantum phase transitions using artificial neural networks on experimental data, Nat. Phys. **15**, 917 (2019).

[23] R. Islam, C. Senko, W. C. Campbell, S. Korenblit, J. Smith, A. Lee, E. E. Edwards, C.-C. J. Wang, J. K. Freericks, and C. Monroe, Emergence and frustration of magnetism with variable-range interactions in a quantum simulator, Science **340**, 583 (2013).

[24] M. Gärttner, J. G. Bohnet, A. Safavi-Naini, M. L. Wall, J. J. Bollinger, and A. M. Rey, Measuring out-of-time-order correlations and multiple quantum spectra in a trapped-ion quantum magnet, Nat. Phys. **13**, 781 (2017).

[25] H. Bernien, S. Schwartz, A. Keesling, H. Levine, A. Omran, H. Pichler, S. Choi, A. S. Zibrov, M. Endres, M. Greiner, V. Vuletić, and M. D. Lukin, Probing many-body dynamics on a 51-atom quantum simulator, Nature (London) **551**, 579 (2017).

[26] J. Zhang, G. Pagano, P. W. Hess, A. Kyprianidis, P. Becker, H. Kaplan, A. V. Gorshkov, Z.-X. Gong, and C. Monroe, Observation of a many-body dynamical phase transition with a 53-qubit quantum simulator, Nature (London) **551**, 601 (2017).

[27] L. D'Alessio, Y. Kafri, A. Polkovnikov, and M. Rigol, From quantum chaos and eigenstate thermalization to statistical mechanics and thermodynamics, Adv. Phys. **65**, 239 (2016).

[28] C. J. Turner, A. A. Michailidis, D. A. Abanin, M. Serbyn, and Z. Papic, Weak ergodicity breaking from quantum many-body scars, Nat. Phys. **14**, 745 (2018).

[29] W. W. Ho, S. Choi, H. Pichler, and M. D. Lukin, Periodic Orbits, Entanglement, and Quantum Many-Body Scars in Constrained Models: Matrix Product State Approach, Phys. Rev. Lett. **122**, 040603 (2019).

[30] M. V. Berry and M. Tabor, Level clustering in the regular spectrum, Proc. R. Soc. London A **356**, 375 (1977).

[31] O. Bohigas, M. J. Giannoni, and C. Schmit, Characterization of Chaotic Quantum Spectra and Universality of Level Fluctuation Laws, Phys. Rev. Lett. **52**, 1 (1984).

[32] E. V. H. Doggen, F. Schindler, K. S. Tikhonov, A. D. Mirlin, T. Neupert, D. G. Polyakov, and I. V. Gornyi, Many-body localization and delocalization in large quantum chains, Phys. Rev. B **98**, 174202 (2018).

[33] S. S. Lee and B. J. Kim, Confusion scheme in machine learning detects double phase transitions and quasi-long-range order, Phys. Rev. E **99**, 043308 (2018).

[34] O. Balabanov and M. Granath, Unsupervised detection of topological quantum state equivalences, arXiv:1908.03469.

[35] S. R. Jain and R. Samajdar, Nodal portraits of quantum billiards: Domains, lines, and statistics, Rev. Mod. Phys. **89**, 045005 (2017).

[36] S. Sridhar, Experimental Observation of Scarred Eigenfunctions of Chaotic Microwave Cavities, Phys. Rev. Lett. **67**, 785 (1991).

[37] V. Milner, J. L. Hanssen, W. C. Campbell, and M. G. Raizen, Optical Billiards for Atoms, Phys. Rev. Lett. **86**, 1514 (2001).

[38] L. A. Ponomarenko, F. Schedin, M. I. Katsnelson, R. Yang, E. H. Hill, K. S. Novoselov, and A. K. Geim, Chaotic Dirac billiard in graphene quantum dots, Science **320**, 356 (2008).

[39] E. J. Heller, Bound-State Eigenfunctions of Classically Chaotic Hamiltonian Systems: Scars of Periodic Orbits, Phys. Rev. Lett. **53**, 1515 (1984).

[40] T. Tao, *Structure and Randomness: Pages from Year One of a Mathematical Blog* (American Mathematical Society, Los Angeles, 2008).

[41] T. Prosen and M. Robnik, Energy level statistics in the transition region between integrability and chaos, J. Phys. A Math. Gen. **26**, 2371 (1993).

[42] W. Beugeling, A. Bäcker, R. Moessner, and M. Haque, Statistical properties of eigenstate amplitudes in complex quantum systems, Phys. Rev. B **98**, 155102 (2018).

[43] Y. Y. Atas, E. Bogomolny, O. Giraud, and G. Roux, Distribution of the Ratio of Consecutive Level Spacings in Random Matrix Ensembles, Phys. Rev. Lett. **110**, 084101 (2013).

[44] K. Sohn, H. Lee, and X. Yan, *Advances in Neural Information Processing Systems* (NIPS, Montreal, Canada, 2015), p. 3483.

[45] D. P. Kingma and M. Welling, *Auto-encoding variational Bayes*, ICLR (2014).

[46] I. Golan and R. El-Yaniv, Deep anomaly detection using geometric transformations, *Adv. Neural Inform. Processing Syst*. 31 (NIPS 2018), p. 9781.

[47] J. An and S. Cho, Variational autoencoder based anomaly detection using reconstruction probability, Special Lecture on IE, 2 (SNU Data Mining Center, Tech. Rep., 2015).

[48] V. Chandola, A. Banerjee, and V. Kumar, Anomaly detection: A survey, ACM Computing Surveys (CSUR) **41**, 15 (2009)

[49] C. Zhang and Y. Chen, Time series anomaly detection with variational autoencoders, arXiv:1907.01702.

[50] M. Cristoforetti, G. Jurman, A. I. Nardelli, C. Furlanello, Towards meaningful physics from generative models, arXiv:1705.09524.

[51] A. Alan Pol, G. Cerminara, C. Germain, M. Pierini, and A. Seth, Detector monitoring with artificial neural networks at the CMS experiment at the CERN Large Hadron Collider, arXiv:1808.00911.

[52] A. Rocchetto, E. Grant, S. Strelchuk, G. Carleo, and S. Severini, Learning hard quantum distributions with variational autoencoders, npj Quantum Inf. **4**, 28 (2018).

[53] C. Gross and I. Bloch, Quantum simulations with ultracold atoms in optical lattices, Science **357**, 995 (2017).

[54] D. Barredo, S. de Leseleuc, V. Lienhard, T. Lahaye, and A. Browaeys, An atom-by-atom assembler of defect-free arbitrary two-dimensional atomic arrays, Science **354**, 1021 (2016).

[55] M. Endres, H. Bernien, A. Keesling, H. Levine, E. R. Anschuetz, A. Krajenbrink, C. Senko, V. Vuletić, M. Greiner, and M. D. Lukin, Atom-by-atom assembly of defect-free one-dimensional cold atom arrays, Science **354**, 1024 (2016).

[56] D. Barredo, V. Lienhard, S. de Léséleuc, T. Lahaye, and A. Browaeys, Synthetic three-dimensional atomic structures assembled atom by atom, Nature (London) **561**, 79 (2018).

[57] S. de Léséleuc, S. Weber, V. Lienhard, D. Barredo, H. P. Büchler, T. Lahaye, and A. Browaeys, Accurate Mapping of Multilevel Rydberg Atoms on Interacting Spin-1/2 Particles for the Quantum Simulation of Ising Model, Phys. Rev. Lett. **120**, 113602 (2018).

[58] D. Peter, S. Mller, S. Wessel, and H. P. Büchler, Anomalous Behavior of Spin Systems with Dipolar Interactions, Phys. Rev. Lett. **109**, 025303 (2012).

[59] A. Chotia, B. Neyenhuis, S. A. Moses, B. Yan, J. P. Covey, M. Foss-Feig, A. M. Rey, D. S. Jin, and J. Ye, Long-Lived Dipolar molecules and Feshbach Molecules in a 3D Optical Lattice, Phys. Rev. Lett. **108**, 080405 (2012).

[60] K. R. A. Hazzard, S. R. Manmana, M. Foss-Feig, and A. M. Rey, Far-From-Equilibrium Quantum Magnetism with Ultracold Polar Molecules, Phys. Rev. Lett. **110**, 075301 (2013).

[61] D. Poilblanc, T. Ziman, J. Bellissard, F. Mila, and G. Montambaux, Europhys. Lett. **22**, 537 (1993).

[62] A. Gubin and L. F. Santos, Quantum chaos: An introduction via chains of interacting spins 1/2, Am. J. Phys. **80**, 246 (2012).

[63] H. J. Wells, Quantum spin chains and random matrix theory, PhD thesis, arXiv:1410.1666.

[64] D. M. Basko, I. L. Aleiner, and B. L. Altshuler, Metal–insulator transition in a weakly interacting many-electron system with localized single-particle states, Ann. Phys. (Amsterdam) **321**, 1126 (2006).

[65] X. Deng, V. E. Kravtsov, G. V. Shlyapnikov, and L. Santos, Duality in Power-Law Localization in Disordered One-Dimensional Systems, Phys. Rev. Lett. **120**, 110602 (2018).

[66] D. P. Kingma and J. Ba, Adam: A method for stochastic optimization, arXiv:1412.6980.

[67] A. W. Sandvik, in *Lectures on the Physics of Strongly Correlated Systems XIV: Fourteenth Training Course in the Physics of Strongly Correlated Systems*, edited by A. Avella and F. Mancini, AIP Conf. Proc. No. 1297 (AIP, New York, 2010), p. 135.

[68] P. Weinberg and M. Bukov, SciPost Phys. **2**, 003 (2017).